

Constraints on Clumps in the Representative Wind of the WN8 Wolf-Rayet star HD 96548 = WR 40 with Simultaneous Broadband Light and Linear-Polarisation Variability

R. Ignace,^{1*} A.F.J. Moffat,^{2,3} C. Robert,^{3,4} and L. Drissen^{3,4}

¹*Department of Physics & Astronomy, East Tennessee State University, Johnson City, TN 37614, USA*

²*Département de physique, Université de Montréal, C.P. 6128, Succ. C-V, Montréal, QC, H3C 3J7, Canada*

³*Centre de Recherche en Astrophysique du Québec, QC, Canada*

⁴*Département de physique, de génie physique et d'optique, Université Laval, Québec, QC, G1V 0A6, Canada*

Accepted XXX. Received YYY; in original form ZZZ

ABSTRACT

We report precision ground-based broadband optical intensity and linear-polarisation light-curves for the sky's brightest WN8 star, WR 40. WN8 stars are notorious for their high level of variability, stemming from stochastic clumps in their strong winds that are slower and less hot than the winds of most other Wolf-Rayet (WR) stars. We confirm previous results that many WR stars display an amplitude of variability that is an order-of-magnitude higher in photometry than in polarimetry. For the first time, the unique nature of near simultaneity of our photometric and polarimetric observations of WR 40 allows us to check whether the two types of variability show correlated behaviour, of which we find none. Assuming simple temporal functions for the brightness and polarisation of individual clumps, a model for simulated light curves is found to reproduce the properties of the observations, specifically the absence of correlation between photometric and polarimetric variations, the ratio of standard deviations for photometric and polarimetric variability, and the ratio of the average intrinsic polarisation relative to its standard deviation. Mapping the solution for time variability to a spatial coordinate suggests that the wind clumps of WR 40 are free-free emitting in addition to light scattering.

Key words: techniques: photometric — techniques: polarimetric — stars: massive — stars: mass-loss — stars: winds, outflows — stars: Wolf-Rayet

1 INTRODUCTION

Wolf-Rayet (WR) stars display strong, fast and hot ionized winds arising from spectral line-driving (Lucy & Abbott 1993; Springmann 1994; Gayley et al. 1995; Nugis & Lamers 2002; Sander & Vink 2020; Vink 2021). The WR spectral classification is associated with three main types of stars (Crowther 2007; Danekhar 2021): (1) main-sequence H-burning stars of very high-mass, above $\sim 60 M_{\odot}$; (2) stars of initial mass $\sim 20\text{--}60 M_{\odot}$ that have evolved to the He-burning stage; and (3) $\sim 15\%$ of the central stars in planetary nebulae with initial masses $\sim 1\text{--}10 M_{\odot}$. Stars of category (1) are essentially all WNh types. Those of category (2) have subclassifications of WN2-9, WC4-9 or WO1-4, all with hydrogen severely depleted or completely absent. For category (3), the stars are mostly [WC/O], strongly dominating in number over [WN]. Among the categories, the binary fraction is high among (1), medium ($\sim 40\%$) among (2) and possibly medium among (3).

Here we concentrate on one well-known star among the second class, HD 96548 = WR 40, with type WN8h¹. It is the brightest in the sky of the WN8 class, which is well known for being the

most intrinsically variable among WR types (Antokhin et al. 1995; Marchenko et al. 1998). Most WN8 stars appear to be single and runaway, likely the result of a SN explosion in a close binary, or slung by close gravitational encounter from a tight young cluster of massive stars (Moffat 1989).

Its relatively high apparent brightness and high level of variability have made WR 40 a frequent target for detailed study. The variability of WR 40 typically at ~ 0.06 mag rms in the optical and with no evidence of periodicity, is understood to be stochastic in nature, originating in its wind clumping (e.g. Ramiaramanantsoa et al. 2019). Contrary to intuition, the intrinsic stochastic photometric variability of WR stars appears to be highest for the slowest winds (or latest subtypes: Lenoir-Craig et al. 2022a). The same applies for spectral line variability (Chené et al. 2020a) and broadband polarimetric variability (Robert et al. 1989). The reason for this trend may be attached to a deeper subsurface Fe convection zone at ~ 170 kK in the cooler WR stars, thus providing more mass and hence larger perturbing gravity waves reaching the stellar hydrostatic surface to generate stochastic wind-clumps (Michaux et al. 2014).

The paper is structured as follows. Section 2 describes our observations of WR 40 obtained in photometry and linear polarimetry, including how the data were corrected for interstellar polarisation. A numerical model for simulating both photometric and polarimetric light curves is presented in Section 3. In this section model pa-

* E-mail: ignace@mail.etsu.edu

¹ WN8 stars are unusual in their properties, and despite some showing evidence for hydrogen, likely belong to category (2) instead of (1).

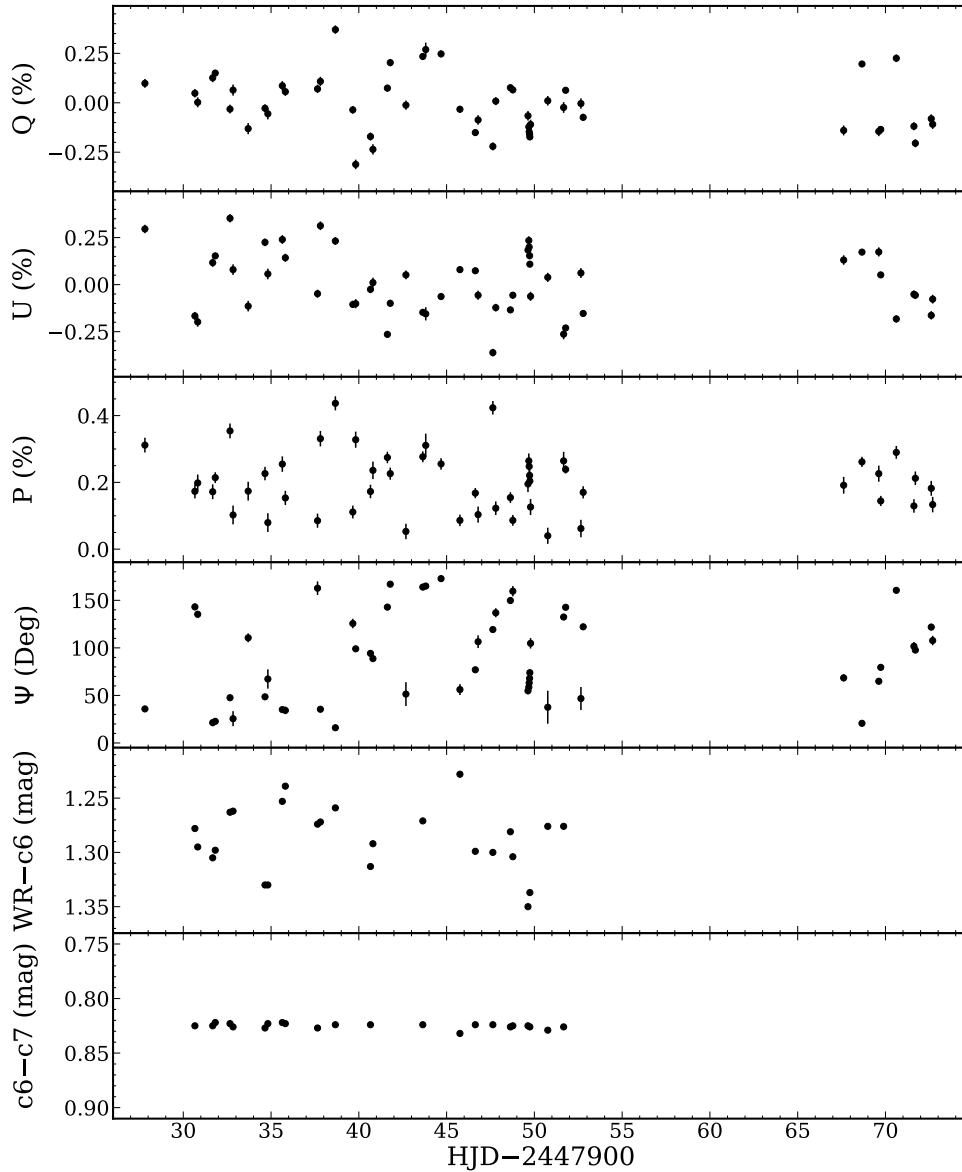


Figure 1. Intrinsic polarisation and differential magnitudes

rameters are set by the requirement of reproducing the statistical characteristics of the observed variability.

2 OBSERVATIONS

Table 1 provides several basic parameters for WR 40: position (RA, DEC), spectral type, magnitude V, colour-index B–V, Gaia EDR3 distance (D) and proper motion (PM), stellar luminosity L_* , mass M_* , radius R_* , and hydrostatic-surface temperature T_* , along with the wind terminal velocity v_∞ and mass-loss rate \dot{M} (according to Simbad and Hamann et al. 2019).

Broadband linear polarimetry was obtained over an interval of 45 days in February/March 1990 with the Minipol polarimeter of the University of Arizona (see St-Louis et al. 1987) attached to the 0.6 m University of Toronto telescope on Las Campanas, Chile (now moved to Cerro Burek as part of el Leoncito Observatory, Argentina). The 52 polarimetric observations (Q_{obs} , U_{obs} , P_{obs} , and Ψ_{obs}) were

obtained on 29 nights (see Tab. 2), spread out in pairs on 18 of those nights and 6 observations on one of the nights. More data from the same observing run were published by Drissen et al. (1992) (WR14, WR25 and WR69) and Robert et al. (1992) (WR6).

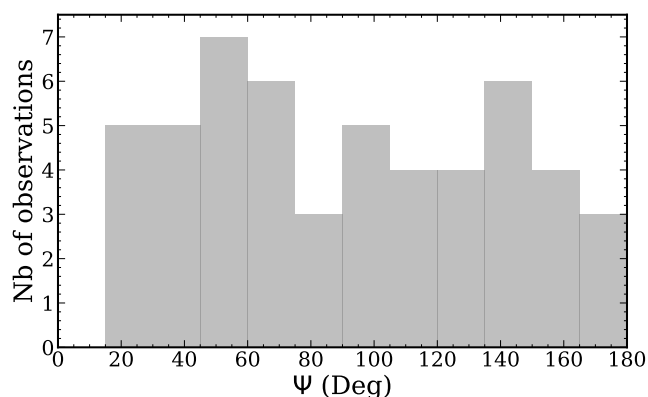
A standard G-band filter (with central wavelength 4640 Å and bandwidth 1280 Å; see Bessell 2005) was used for the polarimetric observations of WR 40. Typical precision of each data-point is $\sigma(P_{\text{obs}}) = \sigma(Q_{\text{obs}}) = \sigma(U_{\text{obs}}) = 0.021\%$. After the gap between HJD 2447952 and HJD 2447967, 0.24 was subtracted from Ψ_{obs} to be consistent with the data before the gap, based on polarised standard stars (HD 110984, HD 111579, HD 126593 and HD 147084; the unpolarised standard stars HD 98161 and 61 Vir have been observed as well).

Differential photometry was obtained also with Minipol relative to two proven constant comparison stars, HD 96568 and HD 96287, noted as c6 and c7 resp. by Lamontagne & Moffat (1987). Observations were obtained on 16 of the 29 nights with 25 measurements, before the 15-day time gap (see Tab. 2). A 0.89 neutral density fil-

Table 1. WR 40 basic parameters

Parameter	Value
RA (J2000)	11:06:17.20
DEC (J2000)	-65:30:35.24
Spectral Type	WN8h
V (mag)	7.70
B-V (mag)	0.10
D (kpc)	2.80 ± 0.13
PM -RA (mas yr ⁻¹)	-2.196 ± 0.018
PM -DEC (mas yr ⁻¹)	-1.745 ± 0.018
$\text{Log}(L_*/L_\odot)$	5.91 ± 0.15
M_* (M_\odot)	28
R_* (R_\odot)	14.5 ± 1.5
T_* (kK)	44.7 ± 3.0
v_∞ (km s ⁻¹) [†]	840 ± 130
\dot{M} (M_\odot yr ⁻¹)	$(6.3 \pm 1.9) \times 10^{-5}$

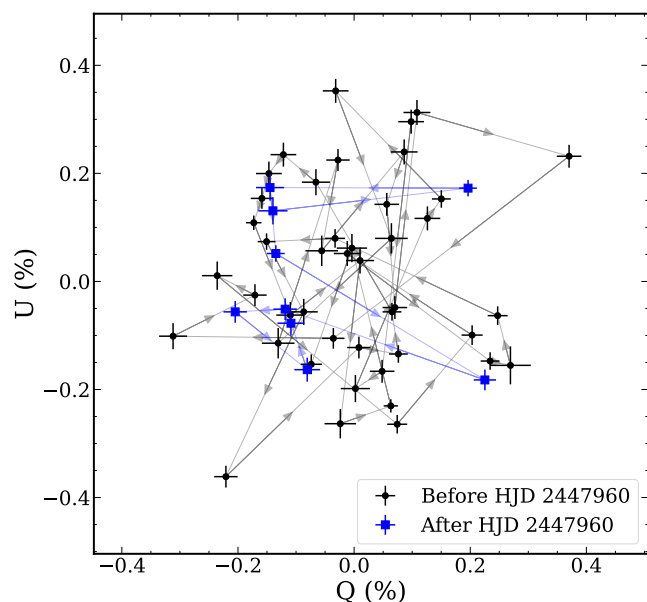
[†] The terminal speed is taken from [Herald et al. \(2001\)](#) and mistakenly reported as 650 km s⁻¹ in [Hamann et al. \(2019\)](#).


Figure 2. Histogram for polarisation position angle Ψ . Note that the observations determine 2Ψ between 0 and 360° , hence Ψ from 0 to 180° .

ter was added to the G-band filter for the photometry. Based on the differences c6–c7, the external error of each photometric data point for WR–c6 is 0.003 mag rms. The typical duration of each photometric data-point was 30 minutes, with the sequence sky–c6–WR–c7–WR–c6–sky, following the 20-minute observation used to secure the polarimetric data. This delay between polarimetry and photometry is negligible compared to the timescale of the intrinsic variations, allowing us to classify the observations as essentially simultaneous.

Figure 1 displays the intrinsic polarimetric parameters Q, U, P, and Ψ and photometric observations WR–c6 and c6–c7 as functions of time. The intrinsic polarisation was obtained after subtraction of the interstellar (ISM) polarisation simply given by the weighted average of all the raw Q_{obs} and U_{obs} values (i.e. $Q_{\text{ISM}} = -0.713 \pm 0.003\%$ and $U_{\text{ISM}} = -1.014 \pm 0.003\%$, or $P_{\text{ISM}} = 1.239 \pm 0.003\%$ and $\Psi_{\text{ISM}} = 117.4 \pm 0^\circ.1$). These values for interstellar polarisation compare well with those derived by [Drissen et al. \(1987\)](#) for WR 40 based on averages of several surrounding field stars.

As shown in Figure 1, Q, U, and P change with time with a maximum peak-to-valley amplitude of $\sim 0.5\%$ through all possible angles between $\Psi = 0$ and 180° (see Fig. 2). The low value in Figure 2 for the smallest angles is likely due to small number statistics. Also, the c6–c7 difference magnitude is quite flat (rms = 0.003 mag),


Figure 3. Intrinsic polarisation Q vs U. The two observing groups are distinguished by different colours. Arrows reflect the observing time-sequence.

confirming the photometric variability of WR 40 with a maximum peak-to-valley amplitude ~ 0.14 mag (and a rms = 0.030 mag).

The random nature of the polarimetric variability is also well illustrated by the Q vs U plot in Figure 3. Arrows in this plot go from one point to the next following the time sequence of the observations. A periodicity search was carried out among the polarimetric and photometric data separately, with negative results, consistent with the later more numerous precision space photometry for WR 40 ([Ramiaramanantsoa et al. 2019](#)). The similarity with the plot shown in Figure 12 of [Drissen et al. \(1987\)](#) is striking, in terms of total amplitude, variability rate and overall shape; these data were obtained with the same equipment as the ones presented here, four years before. Note however the offset caused by the subtraction of the interstellar component in the present paper.

The surprisingly uncorrelated behaviour of the polarimetric vs photometric data is shown in Figure 4. These observations give a ratio of the photometric variation (i.e. standard deviation) over the polarimetric variation $\mathcal{R} = \sigma_m/\sigma_P \approx 27$. Naively, one might expect larger changes in P and smaller changes in magnitude at the stellar limbs and the opposite towards the centre of the star. This will be explored in more detail below.

3 MODEL FOR VARIABLE PHOTOMETRY AND POLARIMETRY

We explore a model to interpret the data presented in the preceding section. A model must account for several properties of the observations. One is that the Q-U plot of Figure 3 is largely a scatter plot, suggestive of two characteristics for the wind structure of WR 40. First, the unresolved star is spherically symmetric in time average. Second, the variability is a stochastic process. If either of these were invalid, one would expect variable polarisation either at fixed position angle, like Be stars with circumstellar disks, or loop patterns traced out in time, as results for binary star systems (cf., Fig. 3 of [Davies et al. 2006](#)).

Table 2. Observations

HJD -2447900	Q _{obs} %	U _{obs} %	P _{obs} %	σ %	Ψ _{obs} Deg	c6-c7 mag	WR-c6 mag
27.793	-0.615	-0.718	0.945	0.022	114.7	—	—
30.640	-0.665	-1.180	1.354	0.021	120.3	0.825	1.278
30.800	-0.711	-1.212	1.405	0.025	119.8	—	1.295
31.654	-0.587	-0.897	1.072	0.022	118.4	0.825	1.305
31.800	-0.563	-0.861	1.029	0.016	118.4	0.822	1.298
32.640	-0.745	-0.661	0.996	0.022	110.8	0.823	1.263
32.814	-0.649	-0.934	1.138	0.028	117.6	0.826	1.262
33.675	-0.844	-1.128	1.409	0.028	116.6	—	—
34.633	-0.741	-0.789	1.083	0.020	113.4	0.827	1.330
34.796	-0.769	-0.957	1.228	0.028	115.6	0.823	1.330
35.620	-0.627	-0.774	0.996	0.023	115.5	0.822	1.253
35.792	-0.657	-0.871	1.091	0.021	116.5	0.823	1.239
37.626	-0.643	-1.062	1.242	0.021	119.4	0.827	1.274
37.789	-0.605	-0.701	0.926	0.023	114.6	—	1.272
38.642	-0.343	-0.782	0.854	0.021	123.0	0.824	1.259
39.636	-0.749	-1.119	1.346	0.019	118.1	—	—
39.800	-1.025	-1.115	1.515	0.024	113.7	—	—
40.642	-0.884	-1.039	1.364	0.020	114.8	0.824	1.313
40.782	-0.949	-1.003	1.381	0.026	113.3	—	1.292
41.605	-0.639	-1.275	1.426	0.017	121.7	—	—
41.768	-0.510	-1.113	1.224	0.018	122.7	—	—
42.661	-0.725	-0.962	1.204	0.023	116.5	—	—
43.622	-0.479	-1.161	1.256	0.016	123.8	0.824	1.271
43.790	-0.444	-1.169	1.251	0.035	124.6	—	—
44.662	-0.466	-1.077	1.173	0.017	123.3	—	—
45.737	-0.746	-0.934	1.195	0.017	115.7	0.832	1.228
46.614	-0.864	-0.940	1.277	0.015	113.7	0.824	1.299
46.772	-0.800	-1.070	1.336	0.024	116.6	—	—
47.613	-0.934	-1.375	1.662	0.020	117.9	0.824	1.300
47.779	-0.705	-1.136	1.337	0.020	119.1	—	—
48.613	-0.637	-1.148	1.313	0.016	120.5	0.826	1.281
48.752	-0.648	-1.070	1.251	0.016	119.4	0.825	1.304
49.615	-0.779	-0.830	1.138	0.024	113.4	0.825	1.350
49.663	-0.835	-0.779	1.142	0.022	111.5	—	—
49.683	-0.860	-0.814	1.184	0.022	111.7	—	—
49.707	-0.872	-0.860	1.225	0.019	112.3	—	—
49.721	-0.886	-0.905	1.267	0.013	112.8	0.826	1.337
49.762	-0.823	-1.076	1.355	0.024	116.3	—	—
50.742	-0.703	-0.975	1.202	0.024	117.1	0.829	1.276
51.646	-0.737	-1.277	1.474	0.027	120.0	0.826	1.276
51.760	-0.650	-1.244	1.404	0.012	121.2	—	—
52.631	-0.717	-0.952	1.192	0.026	116.5	—	—
52.759	-0.787	-1.167	1.387	0.018	118.0	—	—
67.598	-0.853	-0.883	1.228	0.025	113.0	—	—
68.640	-0.517	-0.841	0.987	0.015	119.2	—	—
69.598	-0.858	-0.840	1.201	0.024	112.2	—	—
69.710	-0.848	-0.962	1.282	0.015	114.3	—	—
70.596	-0.488	-1.196	1.292	0.019	123.9	—	—
71.600	-0.832	-1.065	1.352	0.020	116.0	—	—
71.681	-0.918	-1.070	1.410	0.020	114.7	—	—
72.587	-0.794	-1.177	1.420	0.022	118.0	—	—
72.668	-0.822	-1.091	1.366	0.023	116.5	—	—

Other properties involve statistical moments of the light curves. Variations in photometry, Δm , can be defined to have a zero mean with time, and fluctuations about the mean will exhibit the standard deviation σ_m . For the polarimetric variations, while average $\bar{Q} = \bar{U} = 0$, the average polarisation \bar{P} is nonzero, which must be reproduced by the model. Additionally, the fluctuations in the polarisation, σ_P , likewise must be reproduced. The final property of the data is the lack

of correlation between photometric and polarimetric light curves, as shown in Figure 4.

Brown et al. (1995) explored models to reproduce the mean value, fluctuation, and lack of correlation of WR photometric and polarimetric light curves based on non-simultaneous data in the context of wind clumps that were explicitly optically thin to electron scattering. Their models were unable to reproduce the observed ratio $\mathcal{R} \simeq 20$ gathered at the time for WR 40 using the photometric and

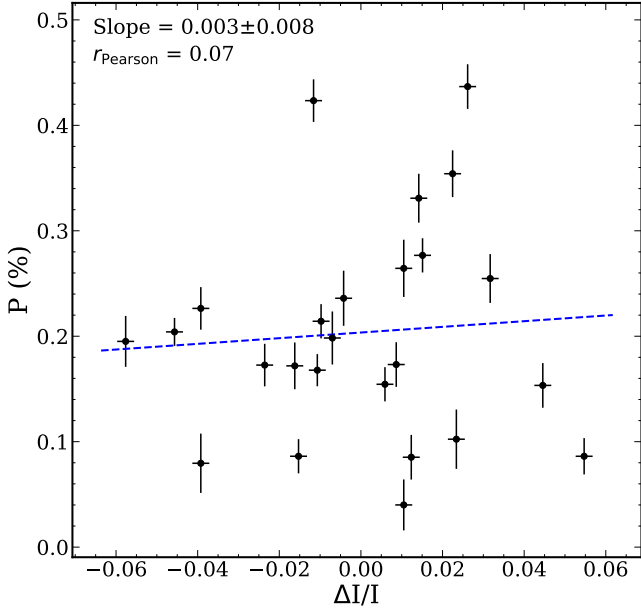


Figure 4. Polarimetric vs photometric data, for simultaneous observations. The photometric data have been converted to relative intensity: $\Delta I/I = -\{(\text{WR-c6}) - (\overline{\text{WR-c6}})\}/1.086$. The blue dotted line is a linear regression fit to the data (the corresponding slope value and Pearson correlation coefficient, r_{Pearson} , are indicated at the top of the plot).

polarimetric data of [Drissen et al. \(1987\)](#) and [Lamontagne & Moffat \(1987\)](#), respectively at different epochs. This ratio was believed to be typical of WR stars in general based on the work of [Robert \(1992\)](#) and [Moffat & Robert \(1992\)](#). The models of [Brown et al. \(1995\)](#) gave lower ratios by a factor of about 4. Interpreting this shortfall, they offered explanations for additional physics consider, along with estimates for quantitative impact: (1) multiple clumps at randomly different positions in the wind, which will reduce the net level of polarisation variability due to geometric cancellation; (2) enhanced recombination emission from clumps due to higher density than outside the clumps in unpolarised light; and (3) multiple scattering within clumps, which will reduce the net polarisation of scattered light off any clump.

[Richardson et al. \(1996\)](#) explored in more detail the effects of considering an ensemble of thin-scattering clumps and reduced the factor of disagreement from $4\times$ to about $3\times$. [Li et al. \(2000\)](#) appear capable of recovering the observed ratio \mathcal{R} through a consideration of wind velocity law effects not included in [Richardson et al. \(1996\)](#); however, those models imply fairly high mass-loss rates of $10^{-4} M_{\odot} \text{ yr}^{-1}$. [Rodrigues & Magalhães \(2000\)](#) considered multiple scattering in thick clumps using Monte Carlo radiative transfer modelling. While it appears that their models can reproduce \mathcal{R} ratios, the results for \bar{P} are too large by about $2\times$, plus no synthetic light curves are presented with relevance for the observed timescale of variability.

We consider a different approach to the problem. In [Ramiamanantsoa et al. \(2019\)](#), a strictly temporal function was adopted for the brightness distribution of an individual clump in WR 40. Simulated light curves were generated to model observations made with BRITE. A match to the statistical characteristics of the measurements, as constrained by the adopted mass-loss rate, led to a brightness amplitude for the clumps, an estimate of clump mass, and inference of a time constant. We extend the approach of [Rami-](#)

[amanantsoa et al. \(2019\)](#) with the inclusion of another temporal function to represent the polarimetric variability, as described next.

3.1 Description of the Model

In [Ramiamanantsoa et al. \(2019\)](#), clumps were assumed to emerge from a pseudo-photosphere formed in the wind, that was the location of continuum formation at optical wavelengths. Assuming a smooth wind, the radius, R_{phot} , of this pseudo-photosphere was estimated from the condition of optical depth unity in electron scattering, noting that electron scattering is linear in density and not subject to the clumping biases that influence density-squared diagnostics (e.g., [Hillier 1991](#); [Hamann et al. 2008](#)). A value of $R_{\text{phot}} \approx 2.4 R_{*}$ was obtained. For the temporal function, we reproduce here Equation 5 from that paper:

$$\frac{f_s}{f_*} = \left(\frac{f_0}{f_*}\right) H(\Delta t) e^{-\Delta t^2/\tau^2}, \quad (1)$$

where f_s is the flux of scattered light by the clump, f_* is the photospheric flux that is considered constant, f_0 is the brightness of the clump at the photosphere, Δt is the travel time in the wind of the clump after emerging from the photosphere, H is the Heaviside function which is zero for $\Delta t < 0$ and unity otherwise, and τ is a free parameter of the model. This time profile function is the declining half of a Gaussian, with half-width at half maximum of $\Delta t_{1/2} = 0.83 \tau$. The function was introduced to fit light-curve measurements of WR 40 obtained with BRITE. A value of $\tau \approx 21.6$ hours was obtained, in the case of all clumps being identical (Case B of that paper; see below).

Another key free parameter for modelling the BRITE data was the injection rate of clumps. Assuming the wind consists entirely of clumps (e.g., [Hillier 2020](#)), the injection rate is related to the mass-loss rate, \dot{M} , of the wind and used to derive clump masses, with

$$\dot{M} = \bar{m}_c \dot{N}, \quad (2)$$

where \bar{m}_c is the average clump mass and \dot{N} is the clump injection rate into the wind. [Ramiamanantsoa et al. \(2019\)](#) considered two types of models: one in which all clumps had the same mass, and one that used a turbulent power-law distribution of clump masses, with progressively more clumps of small mass. Simulated light curves matched the photometric data equally well by both clump models.

Our model involves clumps that emerge from the pseudo-photosphere formed in the wind. Upon emerging, the clump has its peak brightness, which then declines monotonically with time, as the clump moves away from the star. However, for the polarisation the behaviour is different, with a clump having initially zero polarisation. As the clump moves away from the star, the polarisation rises, peaks, and then declines.

This kind of behavior is expected for a uniformly bright stellar atmosphere. [Cassinelli et al. \(1987\)](#) derived the finite star depolarisation factor for thin electron scattering polarisation and showed that polarisation at the photosphere is zero (due to hemispherical isotropy of the illuminating radiation), increases to a peak value at a radius $r_{\text{peak}} > R_{\text{phot}}$, and thereafter declines with larger radius. This behaviour is associated with a uniformly bright atmosphere; the effect of non-uniform stellar surface brightness can change the trend (e.g., [Brown et al. 1989](#)). To replicate qualitatively the case of a uni-

formly bright photosphere, the following form for the flux amplitude of linearly polarised light f_P from a single clump is introduced:

$$\frac{f_P}{f_*} = \left(\frac{f_L}{f_*} \right) H(\Delta t) K \alpha^{-1} (\Delta t / \tau)^\alpha e^{-\Delta t^2 / \tau^2}, \quad (3)$$

where f_L is the peak level of linearly polarised flux, the exponent α is larger than 0, and K is a normalisation constant that depends on the value of α . The required normalisation is given by

$$K \alpha = \alpha^{1/2} e^{-\alpha/2}. \quad (4)$$

To obtain Stokes-Q and U fluxes from an individual clump, a trajectory for the clump must be specified in terms of a position angle on the sky ϕ , and a polar angle θ from the observer axis. We obtain fractional Q and U parameters as

$$Q = \left(\frac{f_P}{f_*} \right) \sin^2 \theta \cos 2\phi, \quad \text{and} \quad (5)$$

$$U = \left(\frac{f_P}{f_*} \right) \sin^2 \theta \sin 2\phi. \quad (6)$$

We define a model run for a duration of time T with a discrete number of clumps N_T . These selections lead to an average injection rate $\dot{N} = N_T / T$. We assign random times for the appearance of each clump at the photosphere as $t_j = s \times T$, where $s \in [0, 1]$ is a random number. The wind is assumed spherically symmetric in time average. This implies that the azimuth has no preferred direction, hence we also sample $\phi = 2\pi \times s$ randomly. Random directions in solid angle require that the polar angle be sampled according to $\cos \theta = -1 + 2s$.

At time t in the synthetic light curve, the scattered light and polarisation properties of the model are determined from:

$$f_{\text{tot}}(t) = \sum_k f_s(\Delta t_k), \quad (7)$$

$$Q_{\text{tot}}(t) = \sum_k Q(\Delta t_k), \quad (8)$$

$$U_{\text{tot}}(t) = \sum_k U(\Delta t_k), \quad (9)$$

$$P(t) = \sqrt{Q_{\text{tot}}^2 + U_{\text{tot}}^2}, \quad (10)$$

$$\tan 2\Psi(t) = \frac{U_{\text{tot}}}{Q_{\text{tot}}}. \quad (11)$$

The random sampling over the light-curve duration, T , leads to a set of times $\{t_k\}$ at which the ensemble of clumps $k = 1, \dots, N_T$ appear at the photosphere. At any time t , the k^{th} clump will have been in the wind for an interval $\Delta t_k = t - t_k$, for those clumps with $\Delta t_k \geq 0$.

We characterise the statistical properties of the simulated light curve with time-averaged values as follows:

$$\bar{f} = \frac{1}{I_{\text{max}}} \sum_1^{I_{\text{max}}} f_{\text{tot}}(t_i), \quad (12)$$

$$\bar{Q} = \frac{1}{I_{\text{max}}} \sum_1^{I_{\text{max}}} Q_{\text{tot}}(t_i), \quad (13)$$

$$\bar{U} = \frac{1}{I_{\text{max}}} \sum_1^{I_{\text{max}}} U_{\text{tot}}(t_i), \quad (14)$$

$$\bar{P} = \frac{1}{I_{\text{max}}} \sum_1^{I_{\text{max}}} P_{\text{tot}}(t_i), \quad (15)$$

where the values $\{t_i\}$ represent the discrete time samples of the model light-curve, of which there are I_{max} measures in total. To be clear, the set $\{k\}$ is an index for the clumps and t_k refers to the times when clumps appear at the R_{phot} (and so are observable); whereas the set $\{i\}$ refers to the synthetic observations and t_i refers to the sampling of the model light curve. The expectation is that for spherical symmetry, both \bar{Q} and \bar{U} will tend toward zero; however, \bar{P} will generally be nonzero (e.g., [Brown et al. 1995](#)). Additionally, the average scattered light \bar{f} is also nonzero, which serves as a bias offset to the assumed non-varying photospheric flux f_* .

Standard deviations associated with light fluctuations for photometry, or flux, and the polarimetry are obtained from the observational dataset and provide constraints for the model. For the synthetic light curves, we introduce standard deviations for the model data as:

$$\sigma_f^2 = \frac{1}{I_{\text{max}}} \sum_1^{I_{\text{max}}} \left[f_{\text{tot}}(t_i) - \bar{f} \right]^2, \quad (16)$$

$$\sigma_Q^2 = \frac{1}{I_{\text{max}}} \sum_1^{I_{\text{max}}} \left[Q_{\text{tot}}(t_i) - \bar{Q} \right]^2, \quad (17)$$

$$\sigma_U^2 = \frac{1}{I_{\text{max}}} \sum_1^{I_{\text{max}}} \left[U_{\text{tot}}(t_i) - \bar{U} \right]^2, \quad (18)$$

$$\sigma_P^2 = \frac{1}{I_{\text{max}}} \sum_1^{I_{\text{max}}} \left[P_{\text{tot}}(t_i) - \bar{P} \right]^2. \quad (19)$$

Additionally, the light-curves are commonly measured in terms of magnitudes, so it is convenient to introduce a magnitude variable, Δm (as distinct from “ m_c ” for clump mass), related to the model fluxes and their variations. Since the average of the flux variations is nonzero, we defined the zero point for the light curve in magnitudes $\Delta m = 0$ as corresponding to the relative flux level $(f_* + \bar{f})/f_* = 1 + \bar{f}/f_*$. Then the light curve in differential magnitude is

$$\Delta m(t) = -2500 \log \left[\frac{f_{\text{tot}}(t)}{f_* + \bar{f}} \right], \quad (20)$$

where the factor of 2500 anticipates, based on the *BRITE* study of WR 40, that differential magnitude will be in milli-magnitudes (mmags). Since $\Delta m = 0$ by definition, the standard deviation of the photometric light curve becomes

$$\sigma_m^2 = \frac{1}{I_{\text{max}}} \sum_1^{I_{\text{max}}} \Delta m_i^2. \quad (21)$$

Finally, it is traditional to use the polarised flux relative to the total light flux to define the polarisation. Our assumption is that the total light is approximately equal to the direct starlight. Equation 3 implies that $P = f_P/f_*$. Similarly, we introduce the scale constant $P_L = f_L/f_*$.

3.2 Simulated Light-Curves

Using the model described in the preceding section, we calculated a suite of simulated light-curves for photometry and polarisation. The synthetic data were evaluated at the sampling of the observations, in terms of both sample size (number of observations) and cadence (temporal sampling). From a given simulation of $\Delta m(t)$ and $P(t)$, we calculate an average polarisation \bar{P} , standard deviation in the polarisation σ_P , and standard deviation in the photometry σ_m .

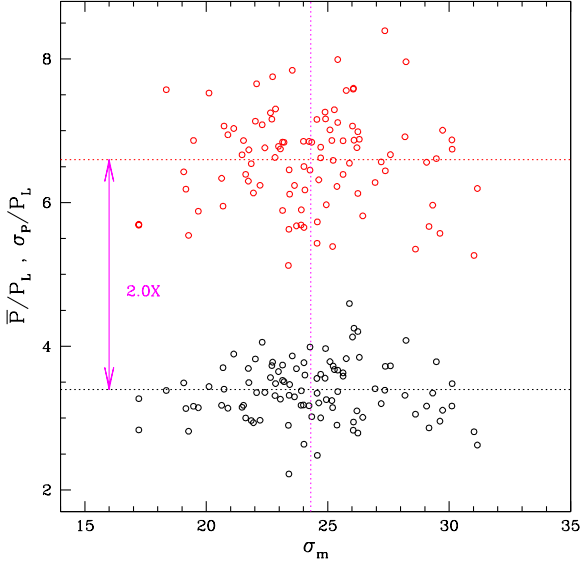


Figure 5. The results of 100 model runs with exponent value of $\alpha = 0.06$ for a wind consisting of identical clumps. The horizontal is the standard deviation in the photometry of the synthetic light curves, σ_m in mmags. The vertical is for the average polarisation: \bar{P} of a light curve relative to the scale constant, P_L , as the red points; the black points are for the standard deviation of the polarised light curves, σ_P , also relative to the scale constant. The lines signify the centroid locations for the two distributions of model runs.

The assumed stochastic nature of the clumped wind means that we cannot evaluate the model by its ability to match each observed data point; instead, we seek to replicate the statistical properties of the data set. This requires us to assess the spread in the statistical properties of the simulations.

Recalling from [Ramiaramanantsoa et al. \(2019\)](#) that Case A models involved a distribution of clump masses, and Case B models involved an ensemble of equal clump masses, we found that both cases gave similar statistical properties for photometric and polarimetric light curves. The addition of polarimetric data does not appear to break this degeneracy reported in the *BRITE* study. While not to imply that clumps do not obey a power-law distribution, we have chosen for simplicity to limit discussion to Case B models of equal-mass clumps in what follows.

We adopt the solution of [Ramiaramanantsoa et al. \(2019\)](#) in terms of clump injection rate \dot{N} and f_0 for the total light variations. For polarimetry the power-law exponent α appears to be a free parameter. However, as seen in [Figure A1](#) from the Appendix, the key diagnostic ratio of \bar{P}/σ_P is largely constant for a wide range in α . To constrain the exponent, we adopt a standard $\beta = 1$ wind velocity law to infer $\alpha \approx 0.06$ (also in the Appendix).

Adopting this value, [Figure 5](#) displays the statistical characteristics for 100 simulated light curves. The horizontal axis is σ_m . The vertical magenta line represents the observed value from the *BRITE* data, and assumes the same time constant, τ , from the study of [Ramiaramanantsoa et al. \(2019\)](#). Red points are for \bar{P} and black points are for σ_P . The model assumes thin electron scattering for the polarisation, which involves a scaling constant P_L that is a free parameter of the model. The data reveal that \bar{P} is about twice as large as σ_P . We require that the observed σ_m is the average of the 100 model runs. The observations show that $\bar{P}/\sigma_P \approx 2.1$. Our models typically produce a ratio of around 2 for a wide range of values in α ; for [Figure 5](#) with $\alpha = 0.06$, the ratio is 2.0 as shown.

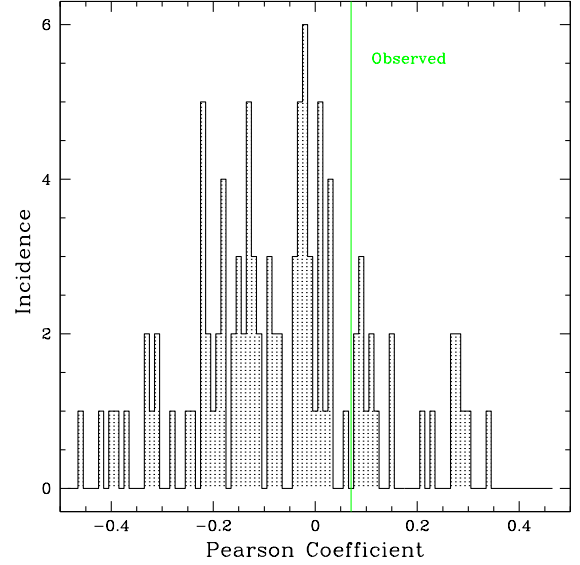


Figure 6. Histogram of Pearson correlation coefficients, r_{Pearson} , computed for Δm versus P for the 100 models used in [Figure 5](#). The vertical green line is the observed value.

Another constraint provided by the data is the relative lack of correlation between polarimetric and photometric variations. Using the Pearson correlation coefficient, [Figure 6](#) shows a histogram for values of r_{Pearson} calculated for the models in [Figure 5](#), as labelled. The vertical green line is the observed value of $r_{\text{Pearson}} = 0.07$ from the observations (cf., [Fig. 4](#)).

While [Figures 5](#) and [6](#) characterise the statistical properties of the model in relation to our data, [Figure 7](#) shows a direct comparison between the data and a randomly selected simulated light curve from the 100 runs in [Figure 5](#). The upper panel compares the observed polarisation (black) against the simulation (red). The lower panel is a plot of the polarisation versus the photometry, again with black for the data and red for the model. The average observed polarisation is $\bar{P} = 0.199\%$; the model average is $\bar{P}/P_L = 6.6$, so $P_L = 0.03\%$ was used to scale the model polarisation light curve to match the mean polarisation of the data.

4 DISCUSSION

To our knowledge, previous observations of stochastic hot-star wind variability have always treated total light and polarimetry separately. Here for the first time we present nearly simultaneous data for these two modes, at least in the majority of the data. This has the advantage of eliminating epoch-dependent differential variability when comparing the two obtained at different epochs, and being able to examine the correlation, if any, between them. One might have expected some level of anti-correlation between the light and polarisation variability. For example, ΔI might be largest and ΔP smallest for clumps coming straight out at us. The reverse is also true, that ΔI would be smallest and ΔP largest for a clump moving orthogonal to our line of sight. However, no correlation is observed.

Our approach has been to employ functions of time for the flux amplitude and polarisation amplitude of individuals clumps. Additionally for polarisation, the trajectory of a clump in θ and ϕ is used for formulating Stokes-Q and U parameters. Simulated light curves

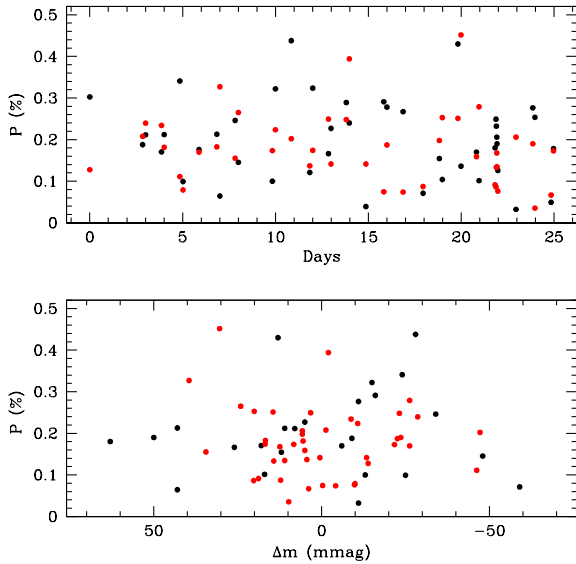
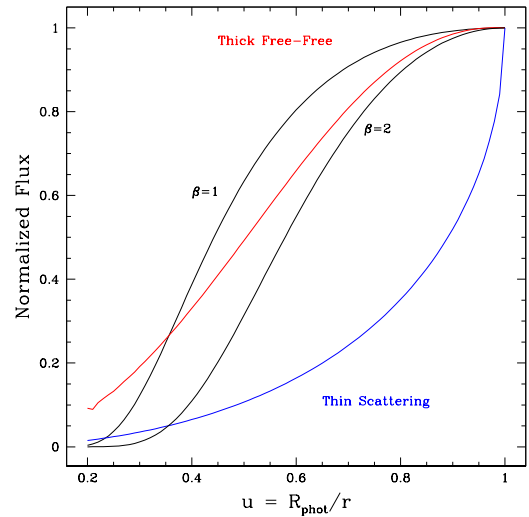


Figure 7. A random model from the 100 runs with statistical properties shown in Figure 5. The upper panel shows the model polarised light curve (red points) at the time sampling of the data (black points). This comparison uses $P_L = 0.03\%$ so that \bar{P} of the model matches that of the light curve. The lower panel displays a plot of both observed and simulated light-curve points in polarisation plotted against the photometric variations.



are obtained by randomly injecting clumps into the wind at the optical pseudo-photosphere, at a rate that maintains the mass-loss rate reported by Hamann et al. (2019).

In Appendix A we show that with selection of a velocity law for the blobs, the time functions for blob evolution can be mapped to radial coordinate. Figure 8 gives an example. The upper panel is for the flux, normalised to the peak value. The lower panel is the polarisation, also normalised to peak value. In both cases curves for the variation in brightness or polarisation for an individual clump are plotted against inverse radius in the wind, $u = R_{\text{phot}}/r$.

Consider first the top panel. The blue curve is for an explicitly thin scattering clump, based on Equations 8 and 10 of Richardson et al. (1996) with $\theta = 90^\circ$. The red curve represents a spherical clump that is optically thick to free-free opacity along its diameter, using Equation 4 of Ignace & Churchwell (2004). For this example an initial optical depth of 2.5 along the diameter was used. Note that in order to maintain a spherical shape and an inverse square density, the radius of the clump, R_c , is assumed to scale with distance in the wind according to $R_c^3 \propto r^2$ (e.g., Ignace 2016). The two black curves are mappings of Equation 1 into inverse radius using a standard β wind velocity law. One curve is for $\beta = 1$ and the other is for $\beta = 2$, as labeled. While neither of the black curves exactly matches the example of a clump optically thick to free-free opacity, both are clearly contrary to the case of a thin scattering clump which displays a precipitous drop in brightness quite near the photosphere.

Shifting to the lower panel of Figure 8 for polarisation, a similar set of comparisons are made. Again, the blue curve is for polarisation from optically thin electron scattering using Equations 7 and 9 from Richardson et al. (1996), also with $\theta = 90^\circ$ as for the blue curve in the upper panel. The curve in magenta is for a clump that is optically thick in electron scattering and is based on the work of Code & Whitney (1995). We make use of Equation 10 and aspects of Equation 11 from that paper. The polarisation for an individual clump expressed

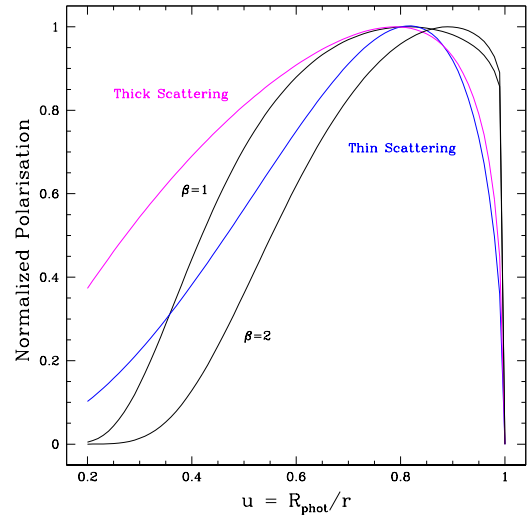


Figure 8. Comparisons between the adopted functions for how individual clumps varying in brightness mapped into the radius coordinate, here displayed as inverse radius ($u = R_{\text{phot}}/r$). Top is for flux normalised to peak, and bottom is for polarisation normalised to peak. At top the blue curve is for a clump that is optically thin to electron scattering, and the red curve is for a clump optically thick in free-free opacity. The two black curves are mappings using the time profile of Equation 1 with $\beta = 1$ and $\beta = 2$ velocity laws. The panel at bottom is similar, except there is no red curve (since free-free does not produce scattering polarisation); instead, the magenta curve is for a clump that is optically thick in electron scattering.

by Equation 11 is normalised by the scattered light from the clump. We adjust that for normalisation by the stellar flux. Additionally, the formulation of those authors does not reduce to polarisation that is linear in electron density when the clump becomes optically thin, so we have included a bridging function to span the thin and thick scattering limits. With these caveats in mind, the magenta curve is for an electron scattering optical depth of initially 2.5 across the diameter of a spherical blob. Again, the two black curves are for the time function of Equation 3, with $\alpha = 0.06$, and $\beta = 1$ and 2. For the polarisation there is some similarity between the black curves and the case of a thin scattering blob, whereas there is less agreement with a blob that is optically thick to electron scattering, where the magenta curve appears to decline much more gradually than the black curves.

The overall impression from the comparisons in Figure 8 is that the total light variation of the clump implied by our model does not seem consistent with optically thin electron scattering. A clump that is optically thick to free-free opacity seems characteristically more consistent with our empirical time function mapped into the radial coordinate for the velocity laws considered. On the other hand, our time function for polarisation is not inconsistent with thin scattering.

Finally some considerations of clumps being all identical or obeying a power-law distribution. Theoretically, various studies suggest that radially and laterally structured flow is to be expected in massive-star winds (e.g., Dessart & Owocki 2002, 2003; Flores et al. 2022; Moens et al. 2022). Empirically, Moffat & Robert (1994) found evidence for a power law distribution of bumps on spectral lines from WR-star winds, each bump assumed to be from one clump (or perhaps a combination of clumps due to so-called "nesting" effects in turbulent jargon). The exponent γ of the power law $N(m_c) \approx m_c^{-\gamma}$ of 1.5 is close to what one observes in Giant Molecular Clouds, where compressible turbulence is known to apply. Our original hope was that we would see a difference in our simulations of constant clump mass vs such a power law. The indifference of the model to the distribution of clump properties suggests our results in this investigation do not depend on such details, but neither can the model provide useful constraints on this aspect of the statistical nature of clumps.

While our modeling does not appear to distinguish between an ensemble of identical clumps versus a power-law distribution of masses, matching the observations does require a different number of clumps overall for the simulation. Modeling the BRITe light curve for WR 40 required about 4× as many identical clumps as compared to the model with a power-law in clump masses (c.f., Tab. 4 of Ramiaramantsoa et al. 2019). This suggests that statistical spatial clustering of identical clumps could perhaps approximate the approach with a diversity of clump properties. The study of Brown et al. (2000) showed that the detailed structure of wind inhomogeneities influences polarization only when of sufficient radial and/or angular² extent. Consequently, clustering of small clumps is expected to act polarimetrically as a single larger clump.

5 CONCLUSIONS

In previous attempts to explain variable brightness and/or polarimetry from WR winds, the approach has generally been to adopt functions of radius motivated by the expected physics. For example regarding the polarisation modelling, some authors adopted optically thin electron scattering for its semi-analytic nature as a convenience

for exploring a broad range of wind and clump parameter space (e.g., Brown et al. 1995; Richardson et al. 1996; Li et al. 2000), while others considered numerically intensive calculations of multiple scattering for a range of clump optical depths but limited to sparse sampling of parameter space (e.g., Code & Whitney 1995; Rodrigues & Magalhães 2000; Townsend 2012). However, while these methods have produced some successes, none have demonstrated success in reproducing simultaneously the properties of the stochastic variability expressed in terms of σ_m , \bar{P} , σ_P , τ , and the apparent absence of correlation between photometric and polarimetric variations.

The study of this paper has focused on interpreting on variable photopolarimetry of the WN8 star WR 40. The WN8 stars are among the coolest WRs with the slowest winds and fit well into the general trend of variability level with WR subtype, whether in spectroscopy (Chéné et al. 2020b), photometry (Lenoir-Craig et al. 2022b), or (broad-band) polarimetry (Robert et al. 1989). The currently best explanation of this trend is subsurface convection, which is deeper, hence denser and more energetic, in cooler WR stars (Michaux et al. 2014), which also have the slowest winds. Among WR stars, WR 40 was selected specifically because of a unique dataset that displays simultaneous photometric and polarimetric variability.

In our interpretative modeling, we chose to extend the work of Ramiaramantsoa et al. (2019) in adopting a temporal function for clump brightness to include variation in polarisation as well. And we find that the observations can, characteristically, be reproduced with such a model, at least in the case of the WN8h star WR 40. The disadvantage of the approach is the apparent detachment from underlying physics governing the clump properties, such as shape or mass. In principle, the two approaches can be bridged, as illustrated by Figure 8. That particular illustration involved the use of a wind velocity law. However, such an approach makes the tacit assumption that a blob retains its character as it moves away from the star. Perhaps the clump evolves, such as fragmenting, colliding with other clumps, or changing shape. Given the reasonable agreement between the measurements and the modeling approach, the time functions that we have adopted can serve to constrain future physical models for structured winds.

ACKNOWLEDGEMENTS

The authors are grateful to an anonymous referee for comments that led to improvements in the manuscript. RI gratefully acknowledges support from the National Science Foundation under Grant No. AST-2009412 and NASA grants HST-GO-15822.002-A and HST-GO-16170.002-A. AFJM, CR, and LD are grateful to NSERC (Canada) for financial support. We thank T. Ramiaramantsoa for the periodicity check.

DATA AVAILABILITY

The data underlying this article are available in the article and in its online supplementary material.

REFERENCES

- Antokhin I., Bertrand J.-F., Lamontagne R., Moffat A. F. J., Matthews J., 1995, *AJ*, **109**, 817
 Bessell M. S., 2005, *ARA&A*, **43**, 293
 Brown J. C., Carlaw V. A., Cassinelli J. P., 1989, *ApJ*, **344**, 341

² Angular extent referring to the angle of the wind structure from the perspective of the stellar source of illumination.

- Brown J. C., Richardson L. L., Antokhin I., Robert C., Moffat A. F. J., St-Louis N., 1995, *A&A*, **295**, 725
- Brown J. C., Ignace R., Cassinelli J. P., 2000, *A&A*, **356**, 619
- Cassinelli J. P., Nordsieck K. H., Murison M. A., 1987, *ApJ*, **317**, 290
- Chené A.-N., St-Louis N., Moffat A. F. J., Gayley K. G., 2020a, *ApJ*, **903**, 113
- Chené A.-N., St-Louis N., Moffat A. F. J., Gayley K. G., 2020b, *ApJ*, **903**, 113
- Code A. D., Whitney B. A., 1995, *ApJ*, **441**, 400
- Crowther P. A., 2007, *ARA&A*, **45**, 177
- Danehar A., 2021, *ApJS*, **257**, 58
- Davies B., Oudmaijer R. D., Vink J. S., 2006, in Kraus M., Miroshnichenko A. S., eds, *Astronomical Society of the Pacific Conference Series Vol. 355, Stars with the B[e] Phenomenon*. p. 173 ([arXiv:astro-ph/0510481](https://arxiv.org/abs/astro-ph/0510481))
- Dessart L., Owocki S. P., 2002, *A&A*, **383**, 1113
- Dessart L., Owocki S. P., 2003, *A&A*, **406**, L1
- Drissen L., St.-Louis N., Moffat A. F. J., Bastien P., 1987, *ApJ*, **322**, 888
- Drissen L., Robert C., Moffat A. F. J., 1992, *ApJ*, **386**, 288
- Flores B. L., Hillier D. J., Dessart L., 2022, *MNRAS*,
- Gayley K. G., Owocki S. P., Cranmer S. R., 1995, *ApJ*, **442**, 296
- Hamann W.-R., Feldmeier A., Oskinoval L., eds, 2008, *Clumping in hot-star winds*
- Hamann W. R., et al., 2019, *A&A*, **625**, A57
- Herald J. E., Hillier D. J., Schulte-Ladbeck R. E., 2001, *ApJ*, **548**, 932
- Hillier D. J., 1991, *A&A*, **247**, 455
- Hillier D. J., 2020, *Galaxies*, **8**, 60
- Ignace R., 2016, *MNRAS*, **457**, 4123
- Ignace R., Churchwell E., 2004, *ApJ*, **610**, 351
- Lamontagne R., Moffat A. F. J., 1987, *AJ*, **94**, 1008
- Lenoir-Craig G., et al., 2022a, *ApJ*, **925**, 79
- Lenoir-Craig G., et al., 2022b, *ApJ*, **925**, 79
- Li Q., Brown J. C., Ignace R., Cassinelli J. P., Oskinoval L. M., 2000, *A&A*, **357**, 233
- Lucy L. B., Abbott D. C., 1993, *ApJ*, **405**, 738
- Marchenko S. V., Moffat A. F. J., Eversberg T., Morel T., Hill G. M., Tovmassian G. H., Seggewiss W., 1998, *MNRAS*, **294**, 642
- Michaux Y. J. L., Moffat A. F. J., Chené A.-N., St-Louis N., 2014, *MNRAS*, **440**, 2
- Moens N., Poniatowski L. G., Hennicker L., Sundqvist J. O., El Mellah I., Kee N. D., 2022, *A&A*, **665**, A42
- Moffat A. F. J., 1989, *ApJ*, **347**, 373
- Moffat A. F. J., Robert C., 1992, in Drissen L., Leitherer C., Nota A., eds, *Astronomical Society of the Pacific Conference Series Vol. 22, Nonisotropic and Variable Outflows from Stars*. p. 203
- Nugis T., Lamers H. J. G. L. M., 2002, *A&A*, **389**, 162
- Ramiaramanantsoa T., et al., 2019, *MNRAS*, **490**, 5921
- Richardson L. L., Brown J. C., Simmons J. F. L., 1996, *A&A*, **306**, 519
- Robert C., 1992, PhD thesis, Université de Montréal, Canada
- Robert C., Moffat A. F. J., Bastien P., Drissen L., St-Louis N., 1989, *ApJ*, **347**, 1034
- Robert C., et al., 1992, *ApJ*, **397**, 277
- Rodrigues C. V., Magalhães A. M., 2000, *ApJ*, **540**, 412
- Sander A. A. C., Vink J. S., 2020, *MNRAS*, **499**, 873
- Springmann U., 1994, *A&A*, **289**, 505
- St-Louis N., Drissen L., Moffat A. F. J., Bastien P., Tapia S., 1987, *ApJ*, **322**, 870
- Townsend R., 2012, in Hoffman J. L., Bjorkman J., Whitney B., eds, *American Institute of Physics Conference Series Vol. 1429, Stellar Polarimetry: from Birth to Death*. pp 278–281. doi:10.1063/1.3701941
- Vink J. S., 2021, arXiv e-prints, p. [arXiv:2109.08164](https://arxiv.org/abs/2109.08164)

APPENDIX A: CONSTRAINING THE EXPONENT α

In the study of WR 40 by [Ramiaramanantsoa et al. \(2019\)](#), the free parameters of the model consisted of the flux amplitude of the clumps

f_0 , the number of clumps N_T , and the timescale for declining brightness of the clump τ . These parameters were constrained by the statistical properties of the variability observed in the *BRITE* light curve for WR 40. The current analysis adds two further parameters α and f_L to model the observed variability in the linear polarisation.

Figure A1 shows model results for several values of the exponent α . The model produces both flux and polarisation light curves at the sampling of the observations. From these the standard deviation in the photometric light curve, σ_m , the average polarisation, \bar{P} , and the standard deviation of the polarisation light curve, σ_P are found and plotted here as black, red, and blue, respectively. The points are the averages for 25 model runs with fixed model parameters, and the error bars represent the standard deviation in those averages.

Of course, the flux variations do not depend on the exponent α ; only polarisation depends on α . The observations reveal that $\bar{P}/\sigma_P \approx 2$. This ratio is approximately achieved for the range of α as shown. Moreover, \bar{P} and σ_P are constant nearly to $\alpha \approx 1$, declining with larger values of α . Thus the observed ratio of \bar{P}/σ_P does not constrain the value of α for the model. The values of \bar{P} and σ_P both involve the scaling constant P_L , which is determined by the data but has no impact on α .

A constraint can be placed on α by the wind velocity. The model for the variation of photometric light from a clump declines monotonically with time; however, the polarised flux starts at zero, rises to a peak, and declines thereafter. This behaviour is reflective of the finite star depolarisation factor of [Cassinelli et al. \(1987\)](#). Considering the scattered polarised light from a clump as a function of radius, this too starts at zero, peaks, then declines. The bridge between these two approaches is the wind velocity which determines the time of flight of a clump from the pseudo-photosphere to the radius at which peak polarisation occurs, and thus the time also.

Using Equation 3, setting $df_P(t)/dt = 0$ gives the time of peak polarisation as

$$t_{\text{peak}} = \sqrt{\frac{\alpha}{2}} \tau. \quad (\text{A1})$$

The radius-dependent formulation for the polarisation involves

$$f_P(r) \propto D(r) r^{-2}, \quad (\text{A2})$$

where $D = \sqrt{1 - R_{\text{phot}}^2/r^2}$ is the finite star depolarisation factor. Peak polarisation is achieved at the location $r_{\text{peak}}/R_{\text{phot}} = \sqrt{3/2} = 1.22$.

Relating the peak in time with the peak in radius is achieved via

$$t_{\text{peak}} = \int_{R_{\text{phot}}}^{r_{\text{peak}}} \frac{dr}{v(r)}, \quad (\text{A3})$$

where $v(r)$ is the wind velocity law. For this we use a standard $\beta = 1$ velocity law with

$$v(r) = v_{\infty} (1 - b R_*/r) = v_{\infty} (1 - b' R_{\text{phot}}/r), \quad (\text{A4})$$

where the second expression renormalises the radius r in terms of the photospheric radius, introducing $b' = b R_*/R_{\text{phot}}$. From $R_{\text{phot}} = 2.4 R_*$ and $b \approx 0.9$, we find $b' \approx 0.4$.

Setting the two expressions for t_{peak} equal and introducing $t_{\infty} = R_*/v_{\infty}$ yields

$$\alpha \approx 1.4 (t_{\infty}/\tau)^2 \approx 0.06. \quad (\text{A5})$$

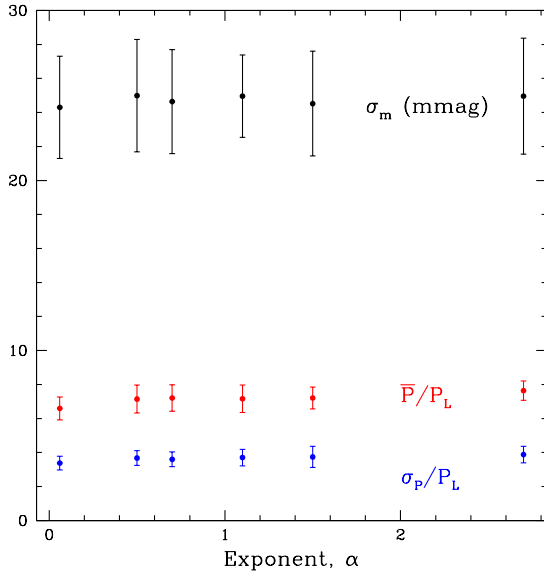


Figure A1. A plot of the statistical properties of simulated light curves with the exponent α . The vertical bars represent the standard deviation for 25 model runs at each of the values of α used. Black is for σ_m which has no functional dependence on α . Red is for the average polarisation \bar{P}/P_L . Blue is for σ_P/P_L . As can be seen, the polarimetric properties are relatively constant below $\alpha = 1$, until α is quite small; for $\alpha > 1$ the red and blue points decline. However, the ratio $\bar{P}/\sigma_P \approx 2$ for the values of α shown.

This paper has been typeset from a $\text{\TeX}/\text{\LaTeX}$ file prepared by the author.